JOURNAL OF GEOPHYSICAL RESEARCH, VOL. 103, NO. B3, PAGES 5143–5163, MARCH 10, 1998

Experimental investigation of silicate-carbonate system at high pressure and high temperature

Isabelle Martinez,[1] Eva Maria Chamorro Peréz, Jan Matas, Philippe Gillet, and Gérard Vidal

Laboratoire des Sciences de la Terre, Ecole Normale Supérieure de Lyon, Lyon, France

Abstract. Melting and subsolidus relations in the $(Mg,Fe)SiO_3$-$(Mg,Fe)CO_3$, $(Mg,Fe)_2SiO_4$-$(Mg,Fe)CO_3$, and $(Mg,Fe)O$-$(Mg,Fe)CO_3$ systems have been investigated at 14, 15, 16 and 25 GPa, 1973 K and 2173 K, using a 1000 t uniaxial multi anvil split sphere apparatus. The iron-magnesium partition coefficients between magnesite and silicates or oxides have been measured in subsolidus assemblages. Iron is always partitioned preferentially in the silicate and oxide phases, the order of increasing partitioning being pyroxene, olivine, silicate perovskite, wadsleyite and magnesiowüstite. A thermodynamic model of iron-magnesium distribution between magnesite and all these phases, based on Gibbs free energy minimization, is established. Melting of pyroxene-magnesite and olivine-magnesite pseudo binary systems is eutectic, with eutectic points close to 1973 K and 60 mol % carbonate at 15 GPa in both systems. In the more complex mantle system, it is likely that such melts would form in the transition zone by heating and homogenization of deep subducted carbonates. The melts formed in the olivine-carbonate system are characterized by high Mg+Fe/Si ratios and thus unlikely to be primary kimberlitic magmas, a conclusion in agreement with previous studies in the peridotite-CO_2 system. On the other hand, the observed pyroxene-magnesite melts formed at transition zone conditions have Mg+Fe/Si ratios that are comparable to those of natural kimberlites, suggesting that melting of carbonated pyroxenites at high pressures could be a source of kimberlitic magmas.

1. Introduction

Thermodynamics and phase relations of silicate-carbonate systems at high pressures and temperatures are essential for understanding the global carbon cycle. Indeed, some carbonate rocks are driven into the deep mantle through subducted slabs [*Becker and Altherr*, 1992], and this mechanism has been proposed for recycling CO_2 in the Earth's mantle [e.g., *Irving and Wyllie*, 1975; *Newton and Sharp*, 1975; *Canil and Scarfe*, 1990; *Katsura and Ito*, 1990; *Biellmann et al.*, 1993]. Although a minor component, CO_2 plays an important role in the Earth's mantle, evidenced by its predominance in volcanic gases, especially at mid-oceanic ridges, the existence of numerous carbonate-rich deep lavas (kimberlites, carbonatites), as well as of carbonate inclusions in xenoliths [*Schiano et al.*, 1994] and solid CO_2 inclusions in diamonds [*Schrauder and Navon*, 1993]. Among the various forms of carbon, carbonates might be an important reservoir for C in the mantle, at least in areas close to subducted slabs. Numerous experimental works have been carried out at high pressure indicating that dolomite is stable down to 100-150 km and magnesite to greater depths [*Kushiro et al.*, 1975; *Brey et al.*, 1983]. From diamond anvil cell experiments, *Biellmann et al.* [1993] concluded that magnesite is the stable carbonate in the presence of mantle silicates up to 50 GPa.

In order to understand the effect of carbonates on melting of silicates at high pressure, we have carried out a series of experiments in a multi anvil press in the $(Mg,Fe)SiO_3$-$(Mg,Fe)CO_3$, $(Mg,Fe)_2SiO_4$-$(Mg,Fe)CO_3$ and $(Mg,Fe)O$-$(Mg,Fe)CO_3$ systems at pressures and temperatures ranging from upper mantle to top of the lower mantle conditions. Previous experiments have been done at similar conditions in the $MgSiO_3$-$MgCO_3$ system by *Katsura and Ito* [1990]; the purpose of the present work is mainly to extend their study to other silicate compositions and to iron-bearing systems. In addition, only a small number of studies have been dedicated to Fe-Mg partitioning between silicates and carbonates [see *Dalton and Wood*, 1993]; such data are important for constraining the effect of Fe on the stability of carbonate minerals at high pressure. We have therefore measured, in this study, the Fe-Mg partitioning between olivine, enstatite, magnesiowustite and magnesite in subsolidus assemblages, as well as the iron-magnesium partitioning between olivine, enstatite and a carbonate-rich melt.

2. Experiments

2.1. Starting Materials

The following assemblages were used as starting materials: (1) synthetic enstatite $MgSiO_3$ + natural siderite $(Fe_{0.7}Mg_{0.3})CO_3$, (2) synthetic pyroxene $(Mg_{0.8}Fe_{0.2})SiO_3$ + natural magnesite $MgCO_3$, (3) natural San-Carlos olivine $(Mg_{0.9}Fe_{0.1})_2SiO_4$ + natural magnesite $MgCO_3$, and (4)

[1] Now at Laboratoire de Géochimie des Isotopes Stables, Institut de Physique du Globe, Paris.

Paper number 97JB03401.
0148-0227/98/97JB-03401$09.00

synthetic periclase MgO + natural siderite $(Fe_{0.7}Mg_{0.3})CO_3$. Electron microprobe analyses, Raman spectroscopy and X ray diffraction indicated that no phases other than those mentioned were detectable. The two phases in each assemblage were first grounded separately in an agate mortar and then mixed in 80-20 silicate-carbonate molar proportion. The mixture was then grounded to reach a good homogeneity and dried at 423 K overnight in vacuum.

2.2. High-Pressure Experiments

Experiments were conducted at 14, 15, 16 and 25 GPa in a 1000 t uniaxial split sphere multianvil apparatus at the Geoinstitut in Bayreuth. Cell assemblies used were 14/8 [e.g., *Schmidt*, 1995] and 7/2 [*McFarlane et al.*, 1994], using semi sintered MgO octahedra with edge lengths of 14 and 7 mm, respectively, as pressure transmitting media, $LaCrO_3$ heaters and Re capsules to contain the samples. Temperatures were monitored with a W-Re 25/3 axial thermocouple for the 14/8 cell, whereas a W-Re 25/3 radial thermocouple was used in the 7/2 cell assemblies. Pressures were calibrated previously, and we refer to *Schmidt* [1995] for the 14/8 assembly, whereas for the 7/2 assembly we used the calibration by *McFarlane et al.* [1994]. In the 14/8 cell assembly, a stepped furnace, thicker at the center, was designed to minimize temperature gradients. Nevertheless, temperature variations in this cell are recorded in the run products which show all the range from subsolidus to liquidus assemblages along the length of the sample capsule. The temperature gradient, symmetric relative to the hottest center of the cell, is estimated to be of the order of 100 K/mm. In the 7/2 assembly, the estimated temperature gradient is probably larger, about 200 K/mm. For a more detailed discussion of pressure and temperature gradients in such experiments, we refer to *Walter et al.* [1995].

In each experiment, pressure was first increased at room temperature to its peak value in 3 to 6 hours and the sample was then heated to the desired temperature over a period of about 20 min. The experiments were maintained at these PT conditions for 1 hour, then quenched to about 500 K in less than 1-2 s by shutting off the electrical power. Even if liquids were produced in the experiments, 1 hour run duration is possible because of the low solubility of Re in those melts. Finally, the pressure was released over a period of 12-15 hours for the 14, 15 and 16 GPa experiments, and 36 hours for the 25 GPa experiments. The run conditions (temperature, pressure, run duration, starting material) are summarized in Table 1.

2.3. Analytical Methods

Recovered samples were mounted in epoxy resin, cut parallel to the main compression axis and polished with alumina paste. They were then studied by scanning electron microscopy (SEM), Raman microprobe and electron probe microanalysis (EPMA). SEM was performed on a JEOL 840A SEM, operating at 25 kV and 3 nA, equipped with a Si(Li) detector for semiquantitative analyses. For quantitative chemical analyses on a Cameca Camebax SX50 microprobe, a beam of 2-3 μm in diameter was used, with an accelerating voltage of 15 kV and a beam current of 10 nA. Acquisition times were 10 s for the major elements and 60 s for minor elements. When analyzing carbonates, a broad raster beam was used (10 μm in diameter) to avoid devolatilization. Since fine dendritic textures formed in the quenched liquid phases, we also used a defocused electron beam to get average compositions of the quenched liquids. Raman spectra were recorded on an XY Dilor Raman microprobe equipped with confocal optics and Argon laser (λ = 514.5 nm) for excitation.

3. Results

3.1. Microstructures and Phases in the Samples

Most samples contain a quenched melt in the hottest part (center of the cell), subsolidus assemblages at the two ends of the capsule, which are thus the coldest parts, and large crystals between subsolidus and melt (Figure 1a). This configuration is due to temperature gradients and then to segregation and migration of melts toward the high- temperature region. The persistence of subsolidus assemblages indicates that these experiments were conducted near the melting point of the assemblage. One should notice that temperatures given in Table 1 and in text are nominal temperatures measured at the coldest point in the 14/8 assembly. They should thus be considered as minimum values, the maximum values in the charge being in the center of the cell and about 150 K above.

Table 1. Summary of the Run Conditions

Run	Temperature, K	Pressure, GPa	Run Duration at Peak Temperature	Estimated Solidus Temperature, K	Starting Material	Products
BT1	1973	15	1 hour	2023	Fs_{20}-Mag	Px+cb+melt
BT2	1973	15	1 hour	2023	Sid_{70}-Ens	Px+cb+melt
BT4	1673-1873	25	1 hour	[a]	Fs_{20}-Mag	Pv+cb
BT6	2173	15	2 min	[a]	Fs_{20}-Mag	Melt
BT8	1973	15	1 hour	2023	Fs_{20}-Mag	Px+cb+melt
BT5	2023	14	1 hour	2023	Fa_{10}-Mag	Ol+cb+melt
BT7	1973	15	1 hour	2023	MgO-Sid_{70}	MgO+cb+melt
BT10	1973	25	0 min	[a]	Fa_{10}-Mag	MgO+Pv
B11	2023	14	1 hour	[a]	Fa_{10}-Mag	Ol+MgO
BT12	2023	14	1 hour	[a]	Fa_{10}-Mag	Ol+wad+cb

Fs, ferrosilite; Mag, magnesite; Fa, fayalite; Sid, siderite; Px, pyroxene; cb, carbonate; ol, olivine; wad, wadsleyite; Pv, perovskite.
[a] Experiments in which no melting was observed.

Table 2a. Quantitative Microprobe Analyses of the Run Products of $(Mg,Fe)SiO_3$-$(Mg,Fe)CO_3$

	Run BT1				
	Quenched Melt		Solidus	Subsolidus	
	Average	Pyroxene	Pyroxene	Magnesite	Pyroxene
n	14	8	18	15	20
SiO_2	36.7(14)	52.3(18)	56.9(4)	-	56.9(3)
MgO	25.1(9)	30.5(2)	33.7(2)	42.4(5)	30.9(7)
FeO	20.5(6)	13.8(4)	8.8(1)	9.9(7)	12.7(11)
Total	81.8(20)	97(17)	99.4(5)	52.3(3)	100.6(2)

	Run BT8				
	Quenched Melt		Solidus	Subsolidus	
	Average	Pyroxene	Pyroxene	Magnesite	Pyroxene
n	12	2	40	7	7
SiO_2	35.5(10)	55.8(3)	57.1(2)	-	55.7(4)
MgO	27.1(5)	32.9(4)	34.0(2)	43.4(8)	31.6(3)
FeO	18.0(5)	10.80(1)	8.0(2)	7.9(14)	11.6(1)
Total	80.6(9)	99.5(7)	99.2(2)	51.2(8)	98.9(2)

	Run BT2				
	Quenched melt		Solidus	Sub-solidus	
	Average	Pyroxene	Pyroxene	Magnesite	Pyroxene
n	13	5	16	17	13
SiO_2	39.1(7)	56.80(13)	57.7(3)	-	57.0(3)
MgO	27.5(5)	33.0(3)	35.6(1)	41.2(3)	32.7(3)
FeO	12.8(2)	8.9(3)	5.33(7)	10.9(3)	9.9(4)
Total	79.4(2)	98.70(13)	98.6(4)	52.1(3)	99.6(1)

	Run BT4 Subsolidus	
	Carbonate	Pyroxene
n	11	13
SiO_2		55.3(3)
MgO	44.8(5)	32.1(3)
FeO	6.5(8)	12(2)
Total	51.3(6)	99.4(4)

In weight percent of oxides; *n* is the number of analyses. Values in parentheses are error bars.

In samples BT1, BT2, BT5 and BT8, subsolidus assemblages consist of small (approximately 10 μm) grains of silicates and carbonates, whereas large silicate crystals (100 μm) are in contact with carbonate-rich melts, which upon quenching formed assemblages of well-isolated silicate domains and intergrowths of very fine-grained magnesite and silicate, with characteristic dendritic microstructures (Figures 1b and 1c). An iron-rich metal phase was also observed in the quenched melt, closely associated to carbonates, and containing some Re coming from the capsule. Using image processing, as described below, we estimate that metal phase occupies about 10% (in volume) of the melt. Whether this metal is due to oxygen loss to the Re capsule or to dismutation of Fe^{2+} into Fe^{3+} + Fe^0 cannot be determined in this study. The

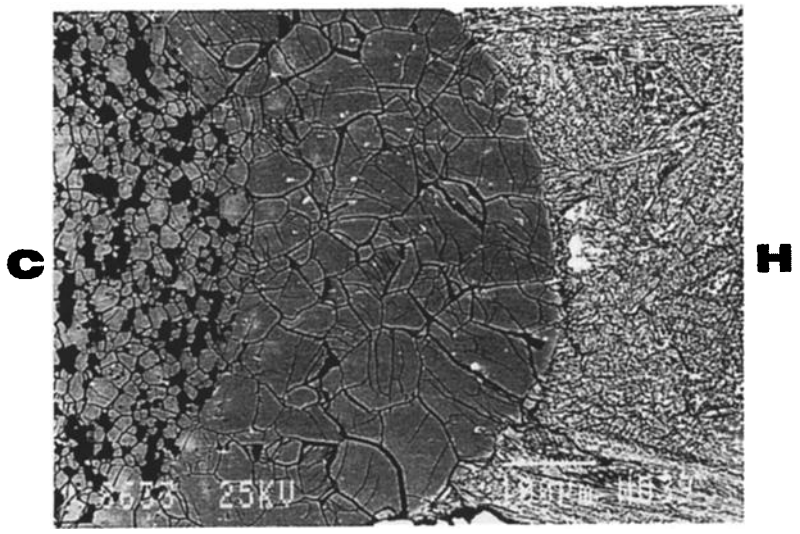

Figure 1a. Back scattered electron image of a half capsule (BT8). C, cold end corresponding to thermocouple reading; H, hot area at the center of the capsule. The sample shows, from left to right: subsolidus assemblages of magnesite (black) and pyroxene (grey), large pyroxene grains and quenched liquid with dendrites.

systematic presence of minor Re in the metallic phase, suggesting that reactions occurred between the carbonatitic liquid and the capsule, is consistent with the first mechanism. Similarly, some Fe-Mo alloys were observed in previous high-pressure melting experiments of peridotite using Mo capsule [*Herzberg et al.*, 1990]. Although the interpretation of the presence of this metallic phase is not straightforward, it might have appeared by exsolution of Fe and Re during cooling of the carbonate-rich melt.

3.1.1. $(Mg,Fe)SiO_3$-$(Mg,Fe)CO_3$ system. Three

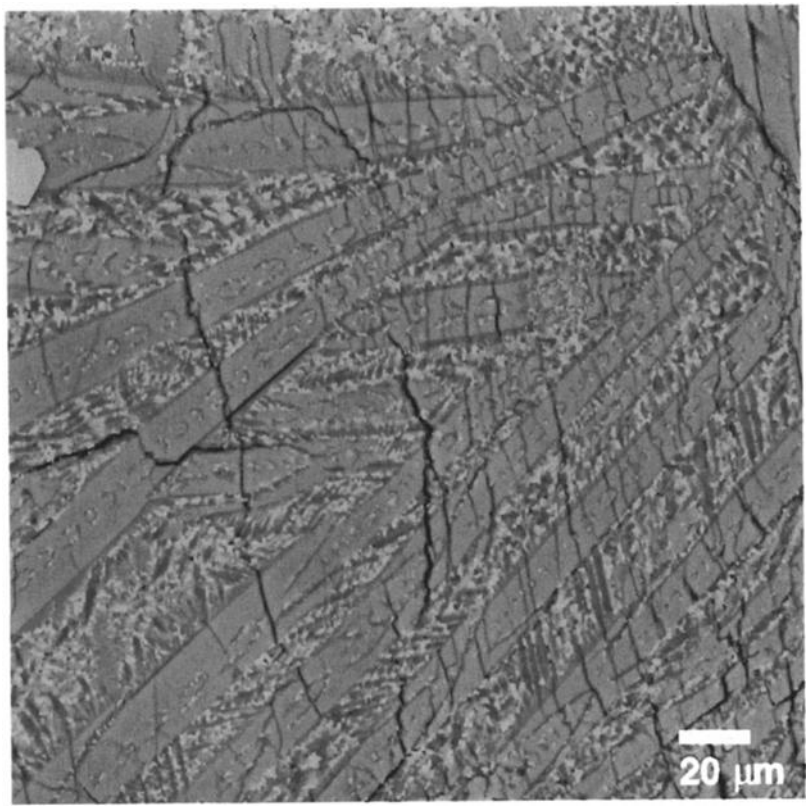

Figure 1b. Back scattered electron image showing two types of lamellae in the quenched liquid in sample BT5: dendritic recrystallization of almost pure olivine lamellae in grey, and lamellae consisting of very fine intergrowths of magnesite (black) + silicate (grey) + Fe-rich metal (white).

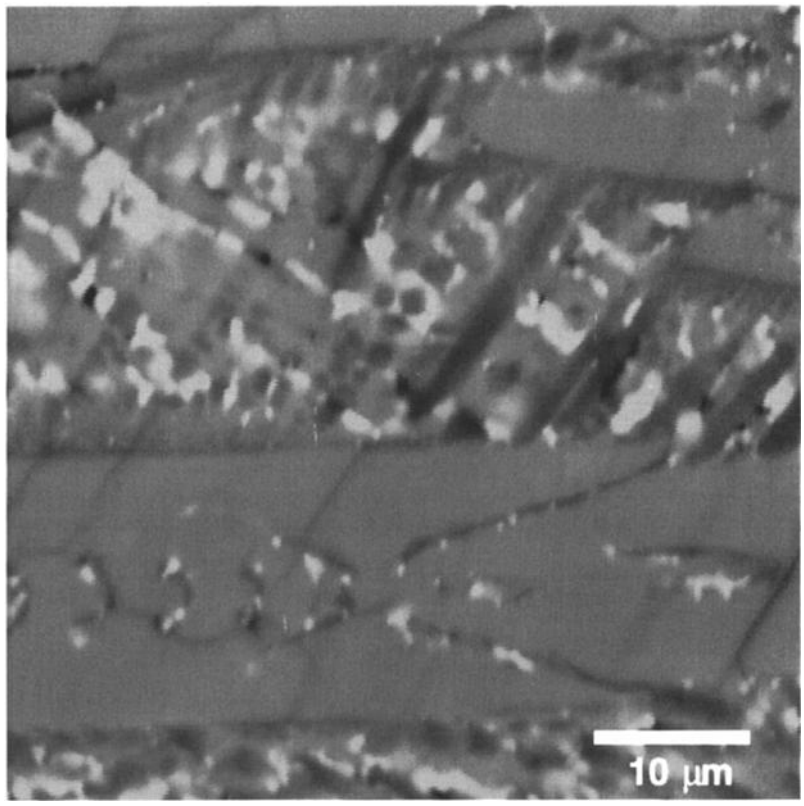

Figure 1c. Detailed view of these two types of lamellae in sample BT5. The olivine-rich lamellae contain a very small fraction of fine intergrowths.

samples were synthesized at 15 GPa and 1973 K (BT1, BT8 and BT2). One sample was synthesized at 15 GPa and 2173 K (BT6) to test for temperature effects, whereas another run was performed at 25 GPa and 1773 K (BT4) to reach the stability field of magnesium silicate perovskite. In this latter experiment, due to thermocouple failure, the run temperature was estimated from power-temperature relationships of previous experiments; the given temperature is therefore less accurate in this run. All the run products are pore-free, at least at the SEM scale, suggesting that no CO_2 was produced during these experiments. Raman spectroscopy of the recovered pyroxenes reveals that they are $P_{21/c}$ clinopyroxene, probably produced by back-transformation of unquenchable $C_{2/c}$ clinopyroxene. In sample BT8, the subsolidus assemblage consists of pyroxene and magnesite crystals of about 20 μm in size, whereas large pyroxene crystals of about 100-150 μm in size are in contact with the quenched melt. No traces of interstitial quenched liquid were observed between the large silicate crystals, most likely because of melt migration toward the hot spot, a phenomenon that is commonly seen in long-duration melting experiments [e.g., *Lesher and Walker*, 1988; *Herzberg et al.*, 1990]. Pyroxene lamellae in the quenched melt are enriched in iron relative to both subsolidus pyroxene crystals and to the large grains in contact with the quenched melt. Average chemical compositions of the run products are reported in Table 2a. Sample BT1, which was produced at the same PT conditions as sample BT8, yields the same chemical compositions. Sample BT2, which represents a reversal experiment of BT1 and BT8, shows the same microstructures, with similar compositions. In these three runs the interface between the subsolidus assemblage and the large pyroxene grains was most likely at the melting temperature, which, taking into account the nominal temperature (1973 K) and the temperature gradient (100 K/mm), was therefore at about 2023 K.

At the same pressure and 2173 K (run BT6), only melt was observed in the capsule. This latter run, however, could be maintained only for 2 min because of thermal instabilities. The 25 GPa sample (BT4) contained only magnesium silicate perovskite and magnesite, coexisting in subsolidus assemblage: no melt was observed in this sample (Figure 2). Some fine-scale microstructures observed within the magnesium silicate perovskite crystals might correspond to twin boundaries, previously described in $(Mg,Fe)SiO_3$ perovskite by several authors [e.g., *Wang et al.*, 1992; *Martinez et al.*, 1997].

3.1.2 $(Mg,Fe)_2SiO_4$-$(Mg,Fe)CO_3$ system. One sample was synthesized at 14 GPa and 2023 K (BT5) in order to compare with the pyroxene-magnesite samples. A second sample was synthesized at 14 GPa and 2173 K (BT11) to test for temperature effects. Two other samples were synthesized at higher pressure, 16 GPa and 1973 K (BT12) to reach the stability field of wadsleyite and 25 GPa-1973 K (BT10) to reach the stability field of magnesium silicate perovskite and magnesiowüstite. Sample BT5 presents the same stratification as observed in the pyroxene-carbonate samples synthesized at similar conditions except that only a very small proportion of subsolidus assemblage could be seen close to the

Table 2b. Quantitative Microprobe Analyses of the Run Products of $(Mg,Fe)_2SiO_4$-$(Mg,Fe)CO_3$

	Run BT5				
	Quenched Melt		Solidus	Subsolidus	
	Average	Olivine	Olivine	Magnesite	Olivine
n	28	31	17	3	3
SiO_2	28.1(6)	41.0(2)	41.4(2)	-	41.0(1)
MgO	38.0(6)	50.2(2)	52.2(2)	46.2(2)	51.7(2)
FeO	13.6(4)	8.6(1)	6.1(2)	4.0(1)	6.7(1)
Total	79.7(9)	99.6(3)	99.7(2)	50.2(2)	99.4(4)

	Run BT11 Solidus		Run BT12			
	Olivine	Oxide	Magnesite	Olivine	Wad	Pyroxene
n	40	9	9	35	30	3
SiO_2	41.80(9)	-	-	40.70(9)	39.0(1)	57.0(3)
MgO	53.8(1)	73.0(7)	46.7(3)	49.6(2)	43.7(2)	37.2(3)
FeO	4.80(3)	23.5(2)	2.0(4)	8.0(1)	14.4(2)	3.72(1)
Total	100.4(1)	96.5(7)	48.7(2)	98.4(2)	97.1(2)	98.0(6)

See Table 2a footnotes.

thermocouple junction, indicating that melting occurred close to the nominal temperature of 2023 K. The relict subsolidus assemblage consists of olivine and magnesite crystals whereas larger olivine crystals, are in contact with the quenched melt. Relatively large lamellae of olivine are observed within the quenched melt, intercalated with mixed lamellae containing fine intergrowths of magnesite and olivine (Figures 1b and 1c). Olivine crystals in the quenched melt are enriched in iron relative to subsolidus crystals and to the large grains in contact with the quenched melt (see Table 2b for chemical analyses).

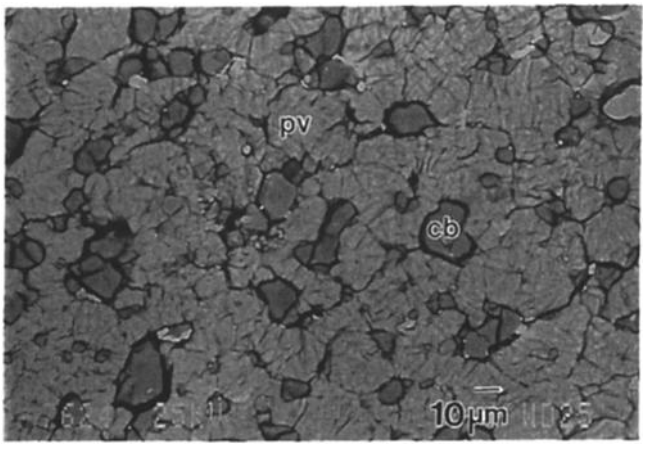

Figure 2. Back scattered electron image of sample BT4, showing $(Mg,Fe)SiO_3$ perovskite in light grey (pv) and magnesite crystals (cb). No melt is present in the sample. Microstructures seen within the perovskite might be due to twinning.

At the same pressure and 2173 K (run BT11), no carbonates could be detected, and only large grains of olivine, containing inclusions of magnesiowüstite, could be observed. The absence of carbon-bearing phases could be explained either by decarbonation or melting to form a carbon-rich fluid which escaped from the capsule, or by carbon solubilization in the silicate phase. Since the presence of magnesiowüstite inclusions is difficult to explain by a simple dissolution mechanism, the first hypothesis seems more likely. The amount of magnesiowüstite is smaller than the initial carbonate proportion, suggesting that the escaping fluid contained some Mg.

A subsolidus assemblage of olivine, wadsleyite (identified by Raman spectrocopy) and magnesite was observed at 16 GPa and 1973 K in sample BT12 (Figure 3). Finally, in sample BT10 (25 GPa, 1973 K), no carbonates could be detected, and

Table 2c. Quantitative Microprobe Analyses of the Run Products of $(Mg,Fe)O$-$(Mg,Fe)CO_3$ for Run BT7

	Solidus	Subsolidus	
		Magnesite	Oxide
n	45	14	12
SiO_2	-	-	-
MgO	72.6(2)	47.9(7)	72.4(2)
FeO	25.3(5)	4.4(5)	27.5(2)
Total	97.9(3) 99.9(3)	52.30(12)	

See Table 2a footnotes.

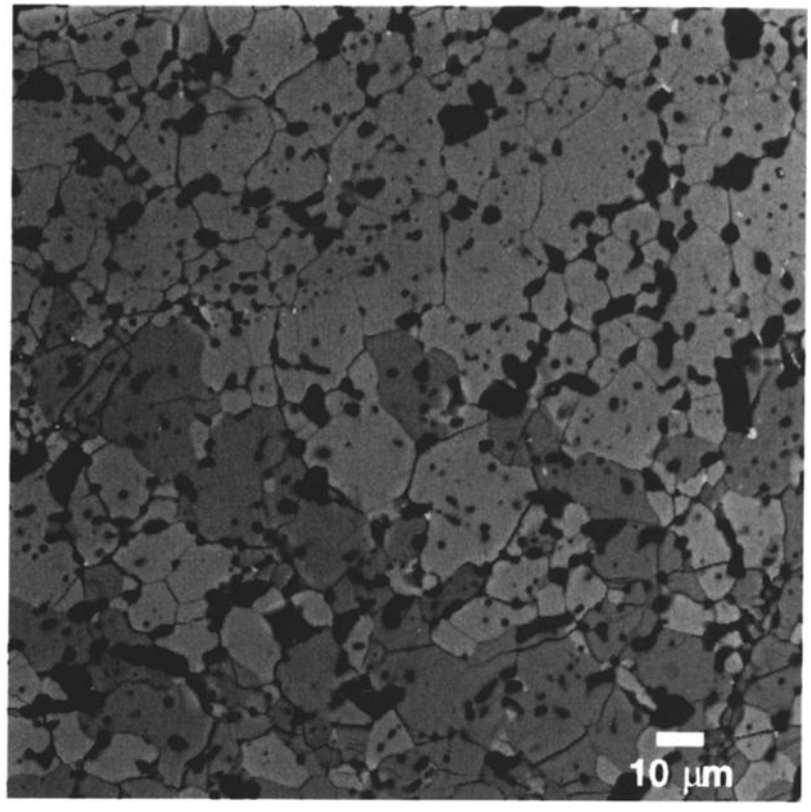

Figure 3. Back scattered electron image of sample BT12: all of the sample consists of subsolidus assemblages of carbonates (in black) and silicate. Both olivine (α-polymorph, in dark grey) and wadsleyite (β-polymorph, in light grey) are present, identified by Raman spectroscopy. No quenched melt is present in this sample.

only magnesium silicate perovskite and magnesiowüstite, coexisting in subsolidus assemblage, were identified. At the hot spots of the sample, homogeneous areas of large magnesiowüstite crystals were observed, probably related to the escape of a fluid through the walls of the capsule, as suggested by the appearance of the Re foil after the experiment.

3.1.3 (Mg,Fe)O-(Mg,Fe)CO_3 system. One sample was synthesized at 15 GPa and 1973 K (BT7). It contains magnesiowüstite and magnesite at the cold end, and, at the hotter end, large magnesiowüstite crystals (up to 100 μm), with residual magnesite, identified by Raman spectroscopy, in grain boundaries (Figure 4). Magnesiowüstite crystals have the same iron content throughout the capsule (see Table 2c for chemical analyses). The textures in this sample resemble those in BT2 and BT8, except that no segregated liquid could be evidenced in the hottest areas of the capsule.

3.2. Iron-Magnesium Partition Coefficients

The iron-magnesium partition coefficient between two phases A and B is defined by

$$Kd_{A\text{-}B} = (Fe/Mg)_A/(Fe/Mg)_B. \quad (1)$$

In the three samples, BT1, BT2 and BT8, pyroxene and magnesite grains that were in direct contact in subsolidus assemblages were analyzed by EPMA to study the iron-magnesium distribution. Possible compositional variations within the grains could not be resolved. The resultant $Kd_{pyroxene\text{-}magnesite}$ values are on average 1.61 (13) in BT1, 1.15 (8) in BT2 and 1.63 (22) in BT8 (Table 3). It should be pointed out that BT2 represents a quasi-reversal experiment of BT1 and BT8, from the point of view of iron-magnesium distribution, even if it has a slightly different bulk iron content. It can thus be safely inferred that $Kd_{pyroxene\text{-}magnesite}$ is between 1.2 and 1.6 at 15 GPa and 1973 K. At 25 GPa, in sample BT4, iron is more partitioned into the silicate phase and an average $Kd_{perovskite\text{-}magnesite}$ value of 2.18 (23) was obtained from chemical analyses of (Mg,Fe)SiO_3 perovskite and adjacent magnesite grains. This value, however, should be taken with caution since zonations were observed in magnesite grains, indicating that chemical equilibrium was not completely attained. In the 15 GPa runs, iron-magnesium distributions are also measured between pyroxene and the coexisting carbonate-bearing melt. The average values of $Kd_{pyroxene\text{-}melt}$ are 0.37 in BT1, 0.31 in BT2 and 0.36 in BT8 (Table 4).

In sample BT5, chemical analyses on adjacent olivine and magnesite crystals near the thermocouple junction yield a value of $Kd_{olivine\text{-}magnesite}$ of 1.50 (30) (Table 3), similar to that measured between pyroxene and magnesite. The derived $Kd_{olivine\text{-}pyroxene}$ is therefore close to 1, in agreement with previous data reported in literature for various PT conditions [*Koch-Müller et al.*, 1992; *von Seckendorff and O'Neill*, 1993; *Takahashi*, 1986]. The average value of $Kd_{olivine\text{-}melt}$ measured in this sample is 0.32 (Table 4), close to $Kd_{pyroxene\text{-}melt}$. Distribution of iron and magnesium between magnesiowustite and carbonate in subsolidus assemblages, measured in sample

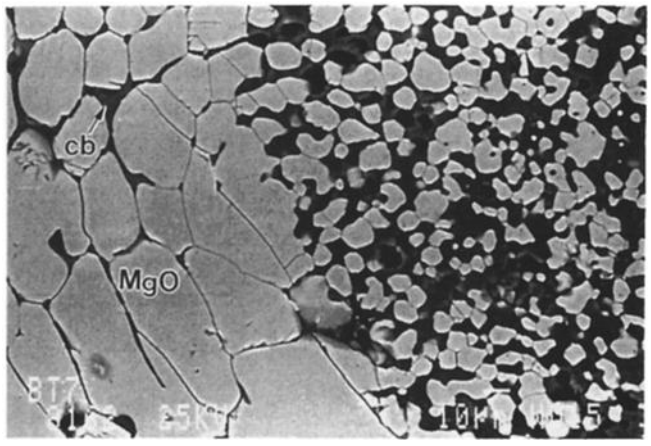

Figure 4a. Back scattered electron images of sample BT7 showing from right to left subsolidus assemblage (magnesiowüstite, in light grey, magnesite, in dark grey) and large magnesiowüstite crystals (labeled MgO) with residual melt (labeled cb).

BT7, leads to an average value of $Kd_{magnesiowüstite\text{-}magnesite}$ of 4.86 (37) (Table 3), showing that iron is strongly partitioned into magnesiowustite. This number falls in the range of $Kd_{magnesiowüstite\text{-}magnesite}$ values obtained in diamond anvil cell experiments performed at 40 GPa by *Biellmann et al.* [1993]. In sample BT12, strong disequilibrium evidences in carbonate grains precluded the measurement of silicate-magnesite partition coefficients, but it was possible to obtain an average value of $Kd_{olivine\text{-}wadsleyite} = 0.47$ (2) (Table 3). It is interesting to compare this result with $Kd_{olivine\text{-}wadsleyite} = 0.57$, obtained by *Katsura and Ito* [1989] in the Mg_2SiO_4-Fe_2SiO_4 system, at 14 GPa and 1873 K, using mantle olivine with a Mg number of 89 as starting material.

3.3. Liquid Compositions

The relative proportions of carbonate and silicate in the quenched melts were determined by point counting of the SEM images. To facilitate visual discrimination of the phases, frequency histograms of the images were computed yielding the number of pixels for each grey level. The distribution displays a classical mixing of discrete Gaussian distributions (one for each phase). Each phase was thus associated on the histogram with a peak value. However, modeling the pixel distribution for one phase by a Gaussian curve would not be relevant as the pixels at the rim of the distribution do not depend on the considered phase only and therefore would not fit in the modelled distribution. To visually discriminate the phases on the image, threshold values were selected on the histogram and applied to the images thus providing a segmented image with enhanced contrast (Figure 5b). At this stage, pixel counting in each class gave its surface fraction in the quenched liquid, which is assumed to be equal to its volume fraction. Average silicate-carbonate contents of the quenched liquids were obtained by processing 10 images sampling different locations. The second step was to eliminate the carbonate-free silicates (pyroxene or olivine) present within the quenched melt (Figure 5c). Pixel counting thus provided the silicate-carbonate proportions of the finest scale intergrowths, as well as the relative proportions of well individualized silicate grains and fine intergrowths.

We paid special attention to the evaluation of the errors

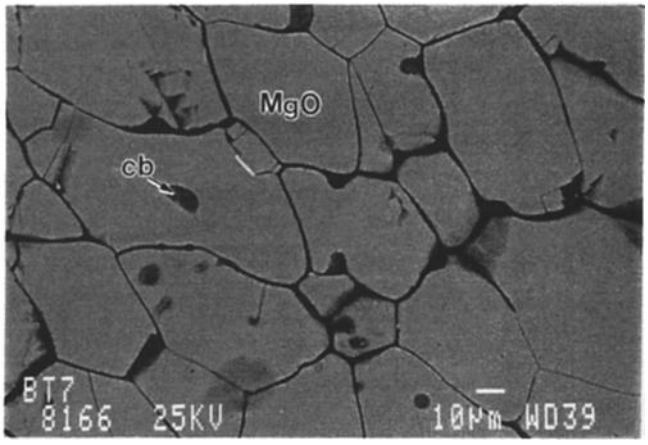

Figure 4b. Magnified view of the large magnesiowüstite crystals with magnesite at grain boundaries and as inclusions.

Table 3. (Fe/Mg) Ratios Reported for Pairs of Silicate/Oxide-Carbonate, as Well as the Calculated Partitioning Coefficient $Kd = (Fe/Mg)_{sil}/(Fe/Mg)_{cb}$

	Sample BT1, $(Mg,Fe)SiO_3$ - $(Mg,Fe)CO_3$											
	1	2	3	4	5	6	7	8	9	10	11	
Fe/Mg atomic% Ens	0.241	0.236	0.230	0.245	0.186	0.245	0.242	0.209	0.227	0.194	0.199	
Fe/Mg atomic% Cb	0.191	0.115	0.121	0.149	0.092	0.157	0.169	0.179	0.140	0.127	0.127	
Kd	1.26	2.05	1.90	1.64	2.02	1.56	1.43	1.17	1.62	1.53	1.57	
Average	1.61											
Standard deviation	0.13											
	Sample BT2, $(Mg,Fe)SiO_3$ - $(Mg,Fe)CO_3$											
	1	2	3	4	5	6	7	8	9	10	11	12
Fe/Mg atomic% Ens	0.118	0.177	0.201	0.199	0 208	0.210	0.169	0.128	0.159	0.161	0.167	0.152
Fe/Mg atomic% Cb	0.131	0.142	0.144	0.165	0.170	0.168	0.142	0.153	0.140	0.130	0.139	0.163
Kd	0.9	1.25	1.39	1.21	1.22	1.25	1.19	0.84	1.13	1.24	1.20	0.93
Average	1.15											
Standard deviation	0.08											
	Sample BT8, $(Mg,Fe)SiO_3$ - $(Mg,Fe)CO_3$											
	1	2	3	4	5							
Fe/Mg atomic% Ens	0.216	0.219	0.198	0.197	0.205							
Fe/Mg atomic% Cb	0.143	0.167	0.114	0.113	0.111							
Kd	1.51	1.31	1.74	1.75	1.85							
Average	1.63											
Standard deviation	0.22											
	Sample BT5, $(Mg,Fe)_2SiO_4$ - $(Mg,Fe)CO_3$											
	1	2	3									
Fe/Mg atomic% Ol	0.071	0.071	0.075									
Fe/Mg atomic% Cb	0.047	0.047	0.051									
Kd	1.51	1.51	1.47									
Average	1.50											
Standard deviation	0.30											
	Sample BT4, $(Mg,Fe)_2SiO_4$ - $(Mg,Fe)CO_3$											
	1	2	3	4	5	6	7					
Fe/Mg atomic% Pv	0.233	0.203	0.234	0.202	0.204	0.220	0.218					
Fe/Mg atomic% Cb	0.091	0.109	0.100	0.123	0.100	0.090	0.089					
Kd	2.56	1.86	2.3	1.64	2.04	2.44	2.45					
Average	2.18											
Standard deviation	0.23											

Table 3. Continued

	1	2	3	4	5	6	7	8	9	10	11	12	13	14	15	16
Sample BT12, $(Mg,Fe)_2SiO_4$ - $(Mg,Fe)CO_3$																
Fe/Mg atomic% Ol	0.0971	0.0991	0.0928	0.1012	0.0965	0.09617	0.0848	0.0795	0.0833	0.0773	0.0735	0.0792	0.0832	0.0917	0.0926	0.0880
Fe/Mg atomic% Wad	0.1719	0.197	0.2068	0.217	0.209	0.2167	0.1861	0.1674	0.1802	0.164	0.1507	0.174	0.195	0.1807	0.1773	0.1806
Kd	0.56	0.50	0.45	0.47	0.46	0.44	0.45	0.47	0.46	0.47	0.49	0.45	0.43	0.50	0.52	0.49
Average	0.47															
Standard deviation	0.02															
Sample BT7, $(Mg,Fe)O$ - $(Mg,Fe)CO_3$																
	1	2	3	4	5	6	7	8	9	10	11					
Fe/Mg atomic% Mw	0.216	0.213	0.210	0.205	0.218	0.213	0.216	0.218	0.218	0.214	0.208					
Fe/Mg atomic% Cb	0.046	0.045	0.038	0.042	0.036	0.066	0.042	0.044	0.044	0.045	0.041					
Kd	4.7	4.7	5.5	4.9	6.0	3.2	5.1	4.9	4.9	4.7	4.9					
Average	4.86															
Standard deviation	0.37															

Ens, enstatite; Cb, carbonate; Ol, olivine; Pv, perovskite; Wad, wadsleyite; Mw, magnesiowüstite.

during the classification process. It is of course impossible to find the true limit for each class, because there is a progressive transition between the phases from a radiometric point of view. Far from the peak, variations of grey levels cannot be directly linked to variations of physical or chemical properties of the surfaces. Those pixels may sample limits between phases corresponding to an unknown percentage of both phases, they may have been sensitive to surface status at the joint or they may vary with three-dimensional shape of transitions. To locate the best limit of each phase among the progressive transition, we produced sequences of images by shifting step by step each limit determined on the histograms. Visual analysis shows that a displacement of five radiometric units produces an obviously false segmentation of the image. This value thus represents the upper bound of the error, and it is more likely that the error is limited to one radiometric unit. This radiometric error can be converted into errors on the surface measurement, the maximum error thus induced being of ±5%. We have also controlled that the error induced by shifting only one limit (i.e., variation of the thickness of one class) did not affect the previous error in greater proportions. A shift of five radiometric units on one limit induces, in the most extreme cases, an error of ± 6% on the surface proportion and in most cases (2/3 of the tests), an error smaller than ± 2%. From this analysis we conclude that the errors on the silicate-carbonate contents in the quenched melts are below 5%.

4. Discussion

4.1. Phase Relations

The bimodal microstructure observed in the quenched melts can be interpreted as a result of isobaric cooling in pseudobinary phase diagrams (Figure 6), similar to that proposed by *Katsura and Ito* [1990]. The large silicate crystals are in equilibrium with the melt (A in Figure 6), whereas the fine intergrowths of magnesite and silicate are the quenched carbonate-rich liquid (B in Figure 6). As already discussed, the quenched liquid actually presents two levels of structural organization: relatively large areas of carbonate-free silicate, coexisting with finer scale intergrowths of carbonate and silicate. These latter areas correspond to the eutectic composition (C in Figure 6), whereas the relatively large areas of carbonate-free silicates correspond to fast crystallization during quench of the melt, which was initially enriched in silicate relative to the eutectic composition. Except for the fact that iron has depressed the eutectic temperature (e.g., 2023 K in this study versus ≈2093 K given by *Katsura and Ito* [1990] for $MgSiO_3$-$MgCO_3$ at 15 GPa), the pseudobinary diagram obtained for $(Mg,Fe)SiO_3$-$(Mg,Fe)CO_3$ is similar to that of *Katsura and Ito* [1990]. In particular, the estimated eutectic composition (63(3) mol % $(Mg,Fe)CO_3$ and 37(3) mol % $(Mg,Fe)SiO_3$) at 15 GPa is in excellent agreement with that of *Katsura and Ito* [1990] (62% mol % $MgCO_3$ and 38 mol % $MgSiO_3$). In the olivine-magnesite system at 14 GPa, the eutectic composition is 60(3) mol % $MgCO_3$ and 40(3) mol % $(Mg,Fe)_2SiO_4$, with a eutectic temperature of 2023 K, close to that measured in the pyroxene-magnesite system. The melting temperature of olivine in presence of magnesite is

Table 4. Iron Distribution Measured Between the Carbonate-Rich Melt and Crystals (Pyroxene or Olivine) in Equilibrium

	Fe/Mg atomic % [a]			FeO wt % [a]		
	Crystals	Melt	*Kd*	Crystals	Melt	*D*
			$(Mg,Fe)SiO_3$ - $(Mg,Fe)CO_3$ System			
BT1	0.146(5), $n = 18$	0.39(2), $n = 5$	0.37	8.8(1)	17.5(2)	0.50
BT8	0.133(3) $n = 40$	0.37(2) $n = 12$	0.36	8.0(2)	18.0(1)	0.44
BT2	0.084(1) $n = 16$	0.26(1) $n = 13$	0.32	5.33(7)	12.84(7)	0.42
			$(Mg,Fe)_2SiO_4$ - $(Mg,Fe)CO_3$ System			
BT5	0.065(2) $n = 17$	0.2(1) $n = 21$	0.33	6.1(2)	13.6(1)	0.45
PL8[b]	-	-	-	4.39	9.47	0.46
FO4[b]	-	-	-	3.05	7.06	0.43

All values are reported in the form of $Kd = (Fe/Mg)_{solid}/(Fe/Mg)_{melt}$ and $D = (FeO)wt\ \%_{solid} / (FeO)wt\ \%_{melt}$; n, number of analyses. For comparison, literature *Kd* and *D* values for olivine-silicate melt CO_2-free systems are also reported.

[a] average values

[b] Samples and Analyses from *Suzuki and Akaogi* [1995]. PL8 and FO4 correspond to two runs they performed at 14 GPa, with San Carlos olivine (Fe/Fe+Mg = 0.1).

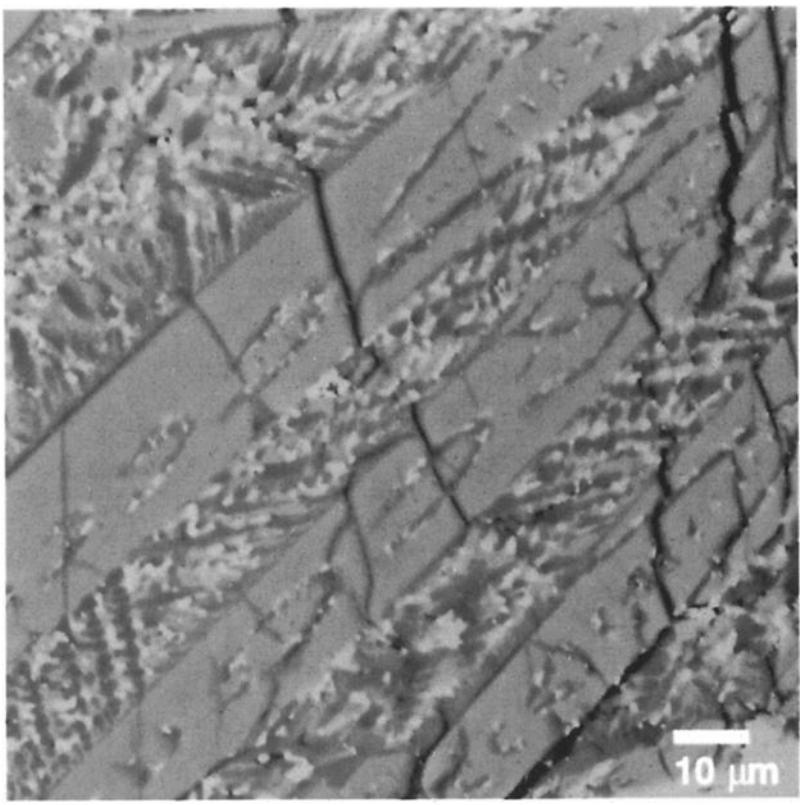

Figure 5a. Back scattered electron image of the quenched melt in sample BT5, given as an example of starting point for image processing (magnification: 1000x).

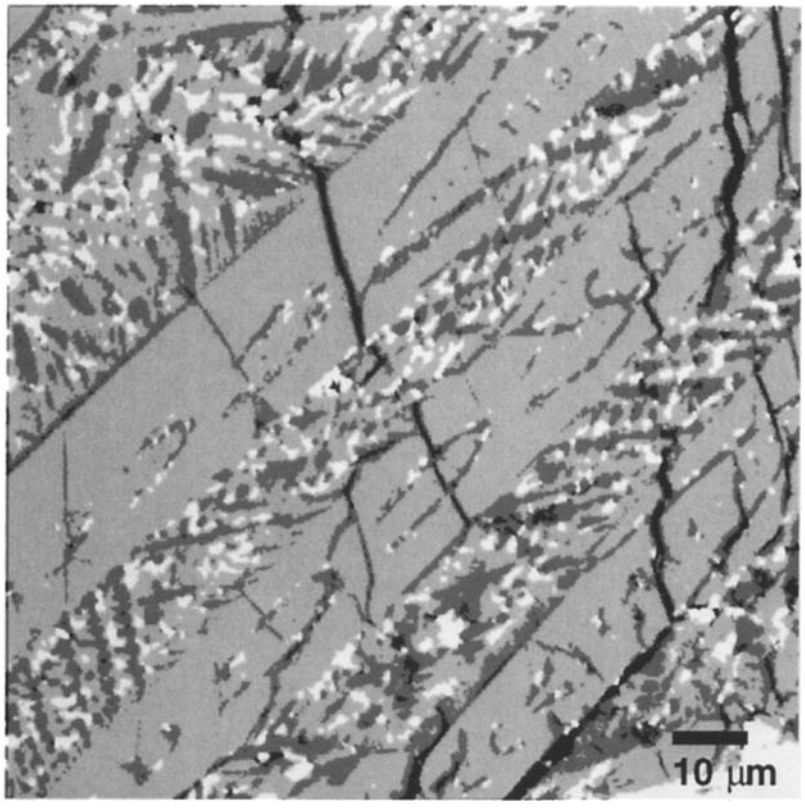

Figure 5b. Corresponding thresholded image. Three phases can be clearly identified: carbonate in dark grey, silicate in light grey and metal in white. Pixel counting in each class yields liquid composition.

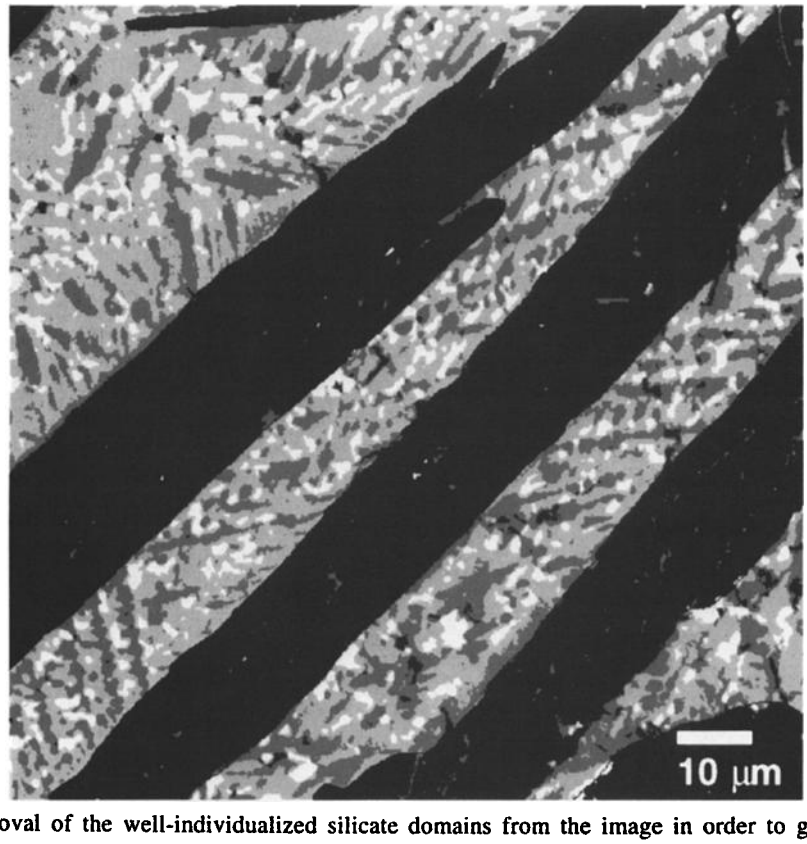

Figure 5c. Removal of the well-individualized silicate domains from the image in order to get the eutectic composition.

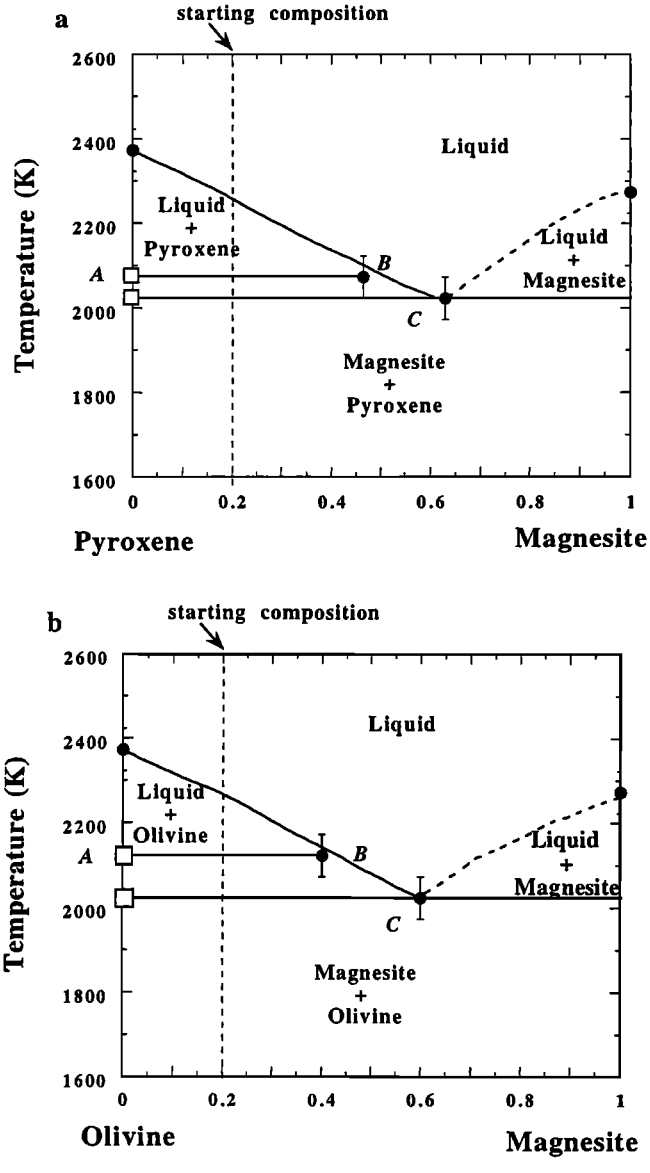

Figure 6. Proposed pseudo binary diagram for (a) $(Mg,Fe)SiO_3$-$(Mg,Fe)CO_3$ at 15 GPa and (b) $(Mg,Fe)_2SiO_4$-$(Mg,Fe)CO_3$ at 14 GPa. Melting points of $(Mg,Fe)SiO_3$ and $(Mg,Fe)CO_3$ are modified after *Presnall and Gasparik* [1990] and *Katsura and Ito* [1990], respectively, by depressing the melting points by about 100 K, for taking into account the effect of iron. Melting point of $(Mg,Fe)_2SiO_4$ is from *Herzberg et al.* [1990]. Points A, B, and C correspond to the different microstructures identified in the sample and are discussed in the text.

considerably lowered relative to pure olivine at the same PT conditions (2023 K compared to 2373 K).

In the magnesiowüstite-magnesite system, the textures are more ambiguous. If melting occurred in this system, the limit of the large magnesiowüstite crystals can be used to estimate a melting point of about 2023 K (Table 1). In this case, the melt has escaped from the capsule, except for some residuals which transformed, upon quench, into magnesite observed in grain boundaries. Since melting evidences are ambiguous in this sample, further experiments should be conducted to verify this hypothesis.

4.2. Iron/Magnesium Partition Coefficients Between Solid Silicates and Magnesite

Our experimental data are used as a starting point for modeling iron-magnesium partitioning between solid silicates and carbonates over a large range of pressure and temperature. The main purpose here is to provide quantitative estimates of pressure and temperature effects on carbonate-silicate iron-magnesium partition coefficients, using available thermodynamic data and phase equilibria. Thermodynamic calculations have been carried out using a numerical code based on minimization of Gibbs free energy [*Matas et al.*, 1996]. The input parameters for the calculation are the bulk chemical composition expressed in the form of oxides (i.e., FeO, MgO, SiO_2 and CO_2), the PT conditions, all the possible components that can exist in the system (solid solutions as well as their end-members), thermochemical data (enthalpies, entropies, heat capacities), thermophysical data (equation of state parameters) and solution parameters for each solid solution. The Gibbs free energy of the system is written as

$$G(P,T,n_1,n_2,\ldots) = \sum n_i \mu_i (P,T,n_i) \quad (2)$$

where P and T are the pressure and temperature, n_i is the mole number of a system component i (here, for example, Mg_2SiO_4, $FeCO_3$...) and μ_i is the chemical potential, which is

$$\mu(P,T,n_i) = \mu^\circ(P,T) + s_i RT \ln(\gamma_i X_i) \quad (3)$$

where s_i is the stoichiometric coefficient of mixing site, and μ_i° is written as

$$\mu^\circ(P,T) = H^\circ_{298} + \int_{298}^{T} C_p dT - TS^\circ_{298} - T\int_{298}^{T} \frac{C_p}{T} dT + \int_1^P V dP \quad (4)$$

If we consider, for example, the olivine solid solution, then the X_i term in the chemical potential is written

$$X^{ol}_{Mg} = \frac{n^{ol}_{Mg}}{n^{ol}_{Mg} + n^{ol}_{Fe}} \quad (5)$$

and using a Margules model for the binary solid solution, we have

$$RT \ln \gamma^{ol}_{Mg} = W_{Mg\text{-}Fe} X^{ol}_{Fe}{}^2$$
$$RT \ln \gamma^{ol}_{Fe} = W_{Fe\text{-}Mg} X^{ol}_{Mg}{}^2 \quad (6)$$

where $W_{Mg\text{-}Fe}$ and $W_{Fe\text{-}Mg}$ are the nonideal mixing parameters in forsterite-fayalite solid solutions. The pressure and temperature dependency of these parameters are expressed in terms of excess enthalpy, excess entropy and excess volume contributions by

$$W = W^H - TW^S + PW^V \quad (7)$$

The dependence of volume on pressure and temperature is given by a high-temperature third-order Birch-Murnaghan equation of state

$$P = \frac{3}{2} K_{0,T} \left[\left(\frac{V_{0,T}}{V} \right)^{7/3} - \left(\frac{V_{0,T}}{V} \right)^{5/3} \right] \times \left\{ 1 + \frac{3}{4} (K'_{0,T} - 4) \left[\left(\frac{V_{0,T}}{V} \right)^{2/3} - 1 \right] \right\} \quad (8)$$

Table 5a. Thermochemical Database Used for Fe-Mg Partitioning Calculations: Standard Enthalpies, Entropies and Heat Capacities

Phases	ΔH°_{298K}, J mol^{-1}	S°_{298K}, J mol^{-1} K^{-1}	Cp (J mol^{-1}) = $a_0 + a_1T + a_2/T^2 + a_3T^2 + a_5/T^3 + a_6T^{0.5} + a_7/T$						
			a_0	a_1	a_2	a_3	a_5	a_6	a_7
Olivine									
Mg_2SiO_4	-2,174,320[a]	94.11[a]	166.99[a]	15.64x10^{-3} [a]	-1.12x10^{7} [a]	0[a]	1.76x10^{9} [a]	0[a]	1,923.9[a]
Fe_2SiO_4	-1,478,170[a]	151[a]	167.00[a]	27.1x10^{-3} [a]	-1.31x10^{6} [a]	0[a]	-2.56x10^{8} [a]	0[a]	-5,561.7[a]
β-phase									
Mg_2SiO_4	-2,141,200[a]	91.72[a]	168.54[a]	13.07x10^{-3} [a]	1.76x10^{5} [a]	0[a]	-6.23x10^{8} [a]	0[a]	-12,226[a]
Fe_2SiO_4	-1,468,000[a]	141.80[a]	168.80[a]	24.03x10^{-3} [a]	-1.72x10^{7} [a]	0[a]	3.15x10^{9} [a]	0[a]	10,552.1[a]
Spinel									
Mg_2SiO_4	-2,131,200[a]	88.02[a]	169.51[a]	11.71x10^{-3} [a]	6.61x10^{6} [a]	0[a]	-1.88x10^{9} [a]	0[a]	-20,906.8[a]
Fe_2SiO_4	-1,471,500[a]	141.03[a]	171.22[a]	27.11x10^{-3} [a]	-6.46x10^{6} [a]	0[a]	1.13x10^{9} [a]	0[a]	-5,471.3[a]
Pyroxene									
$MgSiO_3$	-1,546,290[b]	66.27[b]	144.45[b]	1.88x10^{-3} [b]	-1.35x10^{6} [b]	0[b]	4.61x10^{8} [b]	0	-1.94x10^{4} [b]
$FeSiO_3$	-1,195,200[a]	94.56[a]	131.89[a]	0.06x10^{-3} [a]	-4.95x10^{6} [a]	0[a]	1.42x10^{7} [a]	0[a]	2,319.1[a]
Perovskite									
$MgSiO_3$	-1,442,500[a]	63.58[a]	125.08[a]	6.33x10^{-3} [a]	-736.36x10^{4a}	0[a]	9.1x10^{8} [a]	0[a]	848.43[a]
$FeSiO_3$	-1,090,100[a]	100.77[a]	142.21[a]	1.54x10^{-3} [a]	-1.18x10^{6} [a]	0[a]	2.75x10^{8} [a]	0[a]	-1.45x10^{4} [a]
Magnesiowüstite									
MgO	-601,490[a]	26.94[a]	45.49[a]	4.77x10^{-3} [a]	-2.16x10^{6} [a]	0[a]	1.74x10^{8} [a]	0[a]	2.41x10^{3} [a]
FeO	-267,270[a]	57.59[a]	-16.67[a]	5.67x10^{-2} [a]	-5.32x10^{6} [a]	-1.08x10^{-5} [a]	0[a]	0[a]	3.24x10^{4} [a]
Carbonate									
$MgCO_3$	-1,113,300[c]	64.95[c]	342.09[c]	-6.13x10^{-2} [c]	-1.61x10^{6} [c]	1.40x10^{-5} [c]	3.87x10^{7} [c]	-6.95x10^{3} [c]	5.06x10^{4} [c]
$FeCO_3$	-755,000[c]	95.34[c]	298.35[c]	-3.91x10^{-2} [c]	-1.32x10^{6} [c]	1.00x10^{-5} [c]	2.41x10^{7} [c]	-5.87x10^{3} [c]	4.41x10^{4} [c]

[a] Data from Fei et al. (1991)
[b] Data from Saxena et al. (1993)
[c] From J. Matas (Personal comunication, 1997)

Table 5b. Equation of State Parameters Used for Fe-Mg Partitioning Calculations

Phases	V°_{298}, $cm^3\ mol^{-1}$	$\alpha(T)\ (K^{-1}) = \alpha_1 + \alpha_2 T + \alpha_3 T^2 + \alpha_4 T^{-1}$				K_O GPa	K'_T	$(\partial K_T/\partial T)_P$, GPa K^{-1}
		α_1	α_2	α_3	α_4			
Olivine								
Mg_2SiO_4	43.67[a]	0.31×10^{-4} [a]	0.85×10^{-8} [a]	-0.58[a]	0[a]	128[a]	5.37[a]	-0.022[a]
Fe_2SiO_4	46.28[a]	0.27×10^{-4} [a]	0.87×10^{-8} [a]	-0.25[a]	0[a]	137.9[a]	4[a]	-0.026[a]
β phase								
Mg_2SiO_4	40.54[a]	0.27×10^{-4} [a]	0.69×10^{-8} [a]	-0.58[a]	0[a]	172[a]	4.3[a]	-0.032[a]
Fe_2SiO_4	43.15[a]	0.23×10^{-4} [a]	0.71×10^{-8} [a]	-0.24[a]	0[a]	166[a]	4[a]	-0.021[a]
Spinel								
Mg_2SiO_4	39.65[a]	0.24×10^{-4} [a]	0.53×10^{-8} [a]	-0.57[a]	0[a]	183[a]	4.3[a]	-0.035[a]
Fe_2SiO_4	42.02[a]	0.25×10^{-4} [a]	0.36×10^{-8} [a]	-0.37[a]	0[a]	197[a]	4[a]	-0.037[a]
Pyroxene								
$MgSiO_3$	31.28[b]	3.87×10^{-5} [b]	4.46×10^{-9} [b]	-1.73 [b]	3.43×10^{-4} [b]	107.5 [b]	4.2 [b]	-0.020[b]
$FeSiO_3$	32.95[a]	0.39×10^{-4} [c]	-	-	-	101[a]	4.2[a]	-0.020[a]
Perovskite								
$MgSiO_3$	24.44[c]	1.19×10^{-5} [c]	1.20×10^{-8} [c]	0[c]	0[c]	261[c]	4[c]	-0.027[c]
$FeSiO_3$	25.60[a]	0.26×10^{-4} [a]	1.52×10^{-8} [a]	-0.043[a]	0 [a]	287.2[a]	4[a]	-0.060[a]
Magnesiowüstite								
MgO	11.25[b]	3.64×10^{-5} [b]	8.35×10^{-9} [b]	-0.95 [b]	8.5×10^{-4} [b]	159	4.2	-0.028[b]
FeO	12.25[b]	2.60×10^{-5} [b]	1.47×10^{-8} [b]	-0.43 [b]	2.8×10^{-3} [b]	174	4	-0.020[b]
Carbonate								
$MgCO_3$	28.03[d]	[f]	[f]	[f]	[f]	101[d]	4[d]	-0.015[d]
FeCO3	29.43[d]	[f]	[f]	[f]	[f]	117.3[d]	4[d]	-0.021[d]

[a] Data from *Fei et al.* [1991].
[b] Data from *Saxena et al.* [1993].
[c] Data from *Fiquet et al.* [1997].
[d] From J. *Matas* (personal communication, 1997).
[e] Data from *Sueno et al.* [1976].
[f] Thermal expansion data of carbonates fitted with a different polynomial form from J. *Matas* (personal communication, 1997).

Table 5c. Nonideal Mixing Parameters of Solid Solutions Used for Fe-Mg Partitioning Calculations

Solid Solutions	$W_{Mg\text{-}Fe}$, J/mol	$W_{Fe\text{-}Mg}$, J/mol
Olivine	7120 + 108P [a]	7120 + 108P [a]
β phase	1000 [b]	2000[b]
Spinel	3900 - 1.107[b]	3900[b]
Pyroxene	3420[b]	3420[b]
Perovskite	4130-1.37T+110P[b]	-4050-2.45T+150P[b]
Magnesiowüstite	16100[b]	26300 - 5.56T[b]
Carbonate	3050 - 300P[c]	3050 - 300P[c]

P, gigapascals, T, kelvins.
[a] Data from *Koch-Müller et al.* [1992].
[b] Data from *Fei et al.* [1991].
[c] Parameters that were refined in this work.

where

$$K_{0,T} = K_{0,298K} + \left(\frac{\partial K}{\partial T}\right)_P (T\text{-}298) \qquad (9)$$

and $V_{0,T}$ is calculated with thermal expansion coefficients listed in Table 5b.

For each P and T conditions the code computes the chemical composition of the system at thermodynamic equilibrium, with the constraint of chemical elements conservation. The output is the stable chemical composition at the given P and T conditions. Using the mole numbers of coexisting system components, we have calculated the iron-magnesium partitioning between the desired phases using (1). Input thermodynamic data are all given in Table 5, coming from previous literature data. The nonideality W coefficients in magnesite-siderite solid solutions, however, were adjusted to fit the experimental results obtained in this study.

4.2.1. Olivine-magnesite Fe-Mg partition coefficient. The thermodynamic data used in this calculation for olivine and its polymorphs were first tested by calculating the phase diagram of the (Mg_2SiO_4-Fe_2SiO_4) system at high pressure and temperature. With this data set, the calculated phase diagram is in good agreement with the experimental phase diagram determined by *Katsura and Ito* [1989]. For carbonates, all the thermodynamic data (except for standard enthalpies) were calculated using spectroscopic data (for more details about the technique, see *Guyot et al.*, [1996]) and are given in Table 5.

The results of the calculation are given in Figures 7 and 8. If a mixing parameter $W_{Mg\text{-}Fe} = W_{Fe\text{-}Mg} = 3050 \pm 1500$ J/mol in carbonate is taken from *Dalton and Wood* [1993], the measured Mg-Fe partitioning between olivine and carbonate at 2 GPa and 1273 K is well reproduced (Figure 7a). On the other hand, our measurement at 1973 K and 15 GPa is not well described by this model (Figure 7b). This difference may be due to temperature and/or pressure effects on the W parameters. For example, the sensitivity to a pressure effect on $W_{Mg\text{-}Fe}$ (expressed by adding a W_v term) in magnesite-siderite solid solution is shown in Figures 7a and 7b at 1273 and 1973 K, respectively, whereas the sensitivity to a temperature effect is reported on Figures 7c and 7d. Typically, a value of $W_{Mg\text{-}Fe}$ = 3050 - 300P J/mol would give good agreement between the modeled and experimental values both at 2 and 15 GPa (Figures 7a and 7b). It is clear from Figure 7 that a combination of a pressure and a temperature effect would also give an acceptable fit. In this study we chose to fit the data with a minimum number of adjustable parameters and therefore decided to include a pressure term only. Further data might change the picture and evidence a temperature dependence of W parameter in magnesite-siderite, or more complex pressure and temperature dependencies of W parameters in silicates.

4.2.2. Pyroxene-magnesite Fe-Mg partition coefficient. These data are processed in a similar manner as the olivine/magnesite partitioning data. The nonideal mixing parameter for orthopyroxene is supposed to be independent of P and T; the value is taken from *Koch-Müller et al.* [1992]. With this set of data, we are able to reproduce the experimental values of iron-magnesium partition coefficients between olivine and pyroxene. Then, the calculated iron-magnesium partitioning between orthopyroxene and carbonate is shown in Figure 8b.

4.2.3. (Mg,Fe)SiO_3-perovskite-magnesite Fe-Mg partition coefficient. Only a limited number of thermodynamic data are available for (Mg,Fe)SiO_3-perovskite. To test these data, we first decided to calculate the iron-magnesium partitioning between (Mg,Fe)SiO_3-perovskite and magnesiowüstite which has been measured in the past years [*Katsura and Ito*, 1990; *Martinez et al.*, 1997]. With the database reported in Table 5, the iron-magnesium partition coefficient between silicate perovskite and magnesiowüstite is found to be close to 4 (3.7) at 25 GPa and 1873 K, in close agreement with the value given by *Martinez et al.* [1997]. Calculated iron-magnesium partitioning between (Mg,Fe)SiO_3-perovskite and magnesite is shown in Figure 8c for pressures above 24 GPa, along five different isotherms. The experimental value falls within the calculated range.

4.2.4. Magnesiowüstite-magnesite Fe-Mg partition coefficient. As iron-magnesium partitioning was already calculated for magnesiowüstite-silicate perovskite and silicate perovskite-magnesite equilibria, it is straightforward to obtain $Kd_{magnesiowüstite\text{-}magnesite}$ values. Results are reported in Figure 8d, and a good agreement is found with the experimental value.

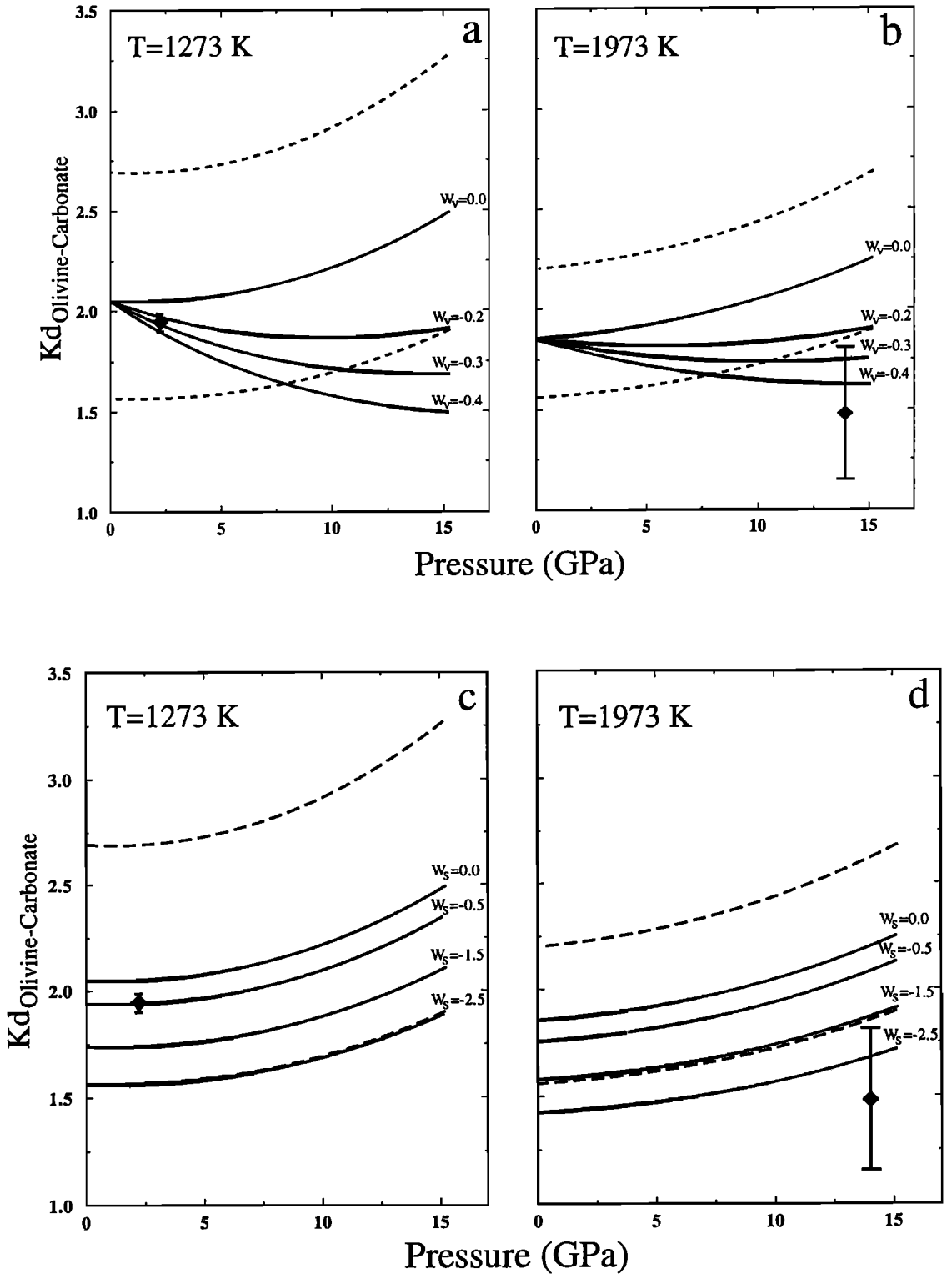

Figure 7. Iron-magnesium partitioning in the olivine-carbonate system, showing the sensitivity to a pressure or temperature effect on $W_{Mg\text{-}Fe}$. Dashed lines correspond to the uncertainty range for the calculations performed with W_v=W_s=0. (a) At 1273 K the pressure dependence is expressed in terms of an excess volume contribution (W_v) varying from 0 to -0.4 kJ/mol. Within the error bar, any of the W_v values investigated is able to reproduce the experimental *Kd* measured at 2 GPa by *Dalton and Wood* [1993]. (b) At 1973 K a negative excess volume term adequately reproduces the experimental *Kd* measured at 15 GPa in this study. (c) and (d) Effect of a temperature dependence, expressed in terms of an excess entropy contribution (W_s) on $Kd_{\text{olivine-carbonate}}$ at 1273 K and 1973 K, respectively.

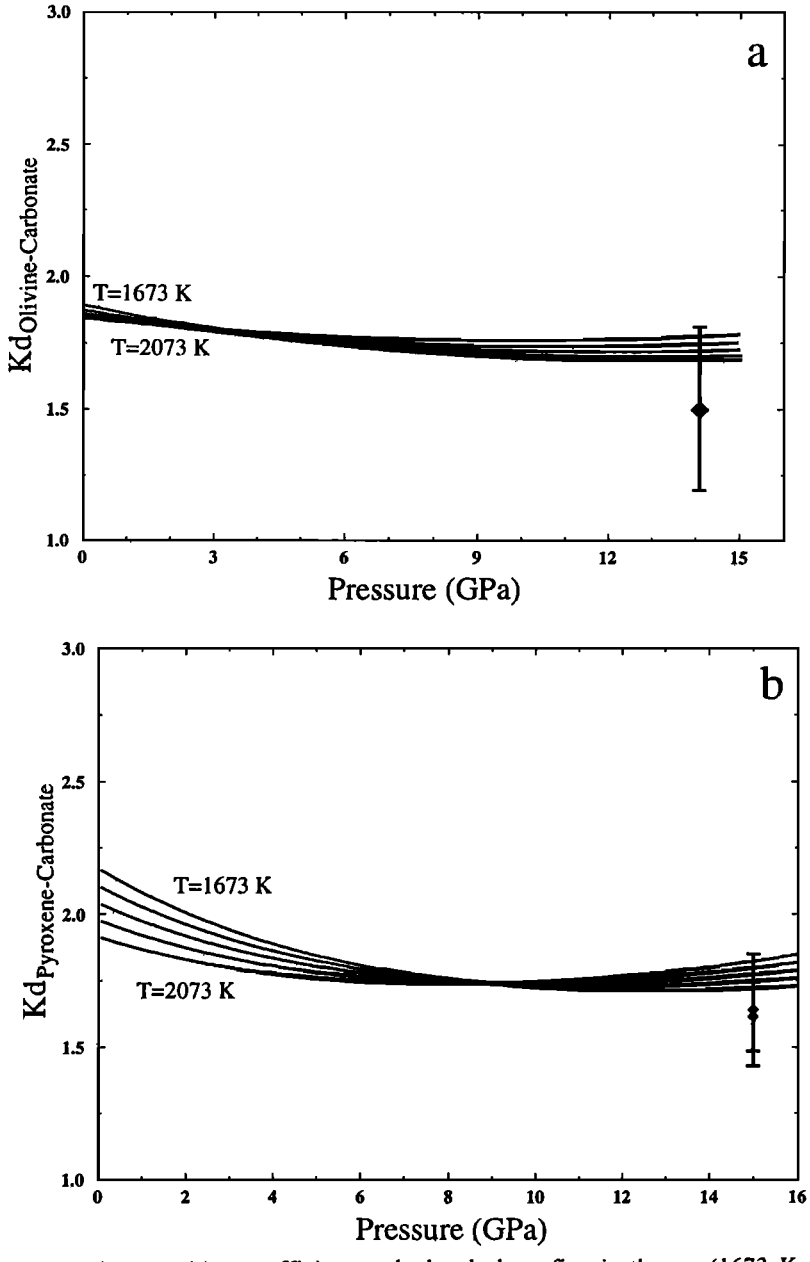

Figure 8. Iron-magnesium partition coefficients calculated along five isotherms (1673 K to 2073 K every 100 K), as a function of pressure, with a selected set of thermodynamic parameters (see text). Experimental points are from this study. (a) Olivine-carbonate, (b) pyroxene-magnesite, (c) silicate perovskite-magnesite, (d) magnesiowüstite-magnesite.

4.3. Iron/Magnesium Partitioning Between Solid Silicates and Carbonate-Rich Melts

Numerous measurements of iron-magnesium distribution between olivine and silicate melt have been performed in CO_2-free systems [e.g., *Takahashi*, 1986; *Suzuki and Akaogi*, 1995; *Herzberg and Zhang*, 1996]. In this study we obtain a value of $Kd_{olivine\text{-}melt} = 0.33$ (or D=0.45) between olivine and carbonate-rich silicate melt in BT5. This value is quite close to the values of $D = 0.46$ for the synthetic olivine and $D = 0.43$ for San Carlos olivine at 14 GPa and 2673 K [*Suzuki and Akaogi*, 1995] and $Kd = 0.37$ at 14 GPa and 2173 K [*Takahashi*, 1986]. Although more data are clearly needed, these results suggest that the presence of CO_2 in the melt does not strongly affect the high-temperature, high-pressure Fe-Mg mineral-melt partitioning.

4.4. Implications for Carbonate Stability in the Mantle and Generation of Kimberlitic Magmas

As shown by several authors [e.g., *Brey et al.*, 1983; *Biellmann et al.*, 1993], magnesite is likely to be the major solid carbonate carried by subduction at great depths in the mantle, since calcite and dolomite progressively lose their calcium at the expense of pyroxenes as pressure increases. As also reported in literature [e.g., *Martinez et al.*, 1995], the carbonates are very stable versus CO_2 loss at high pressures.

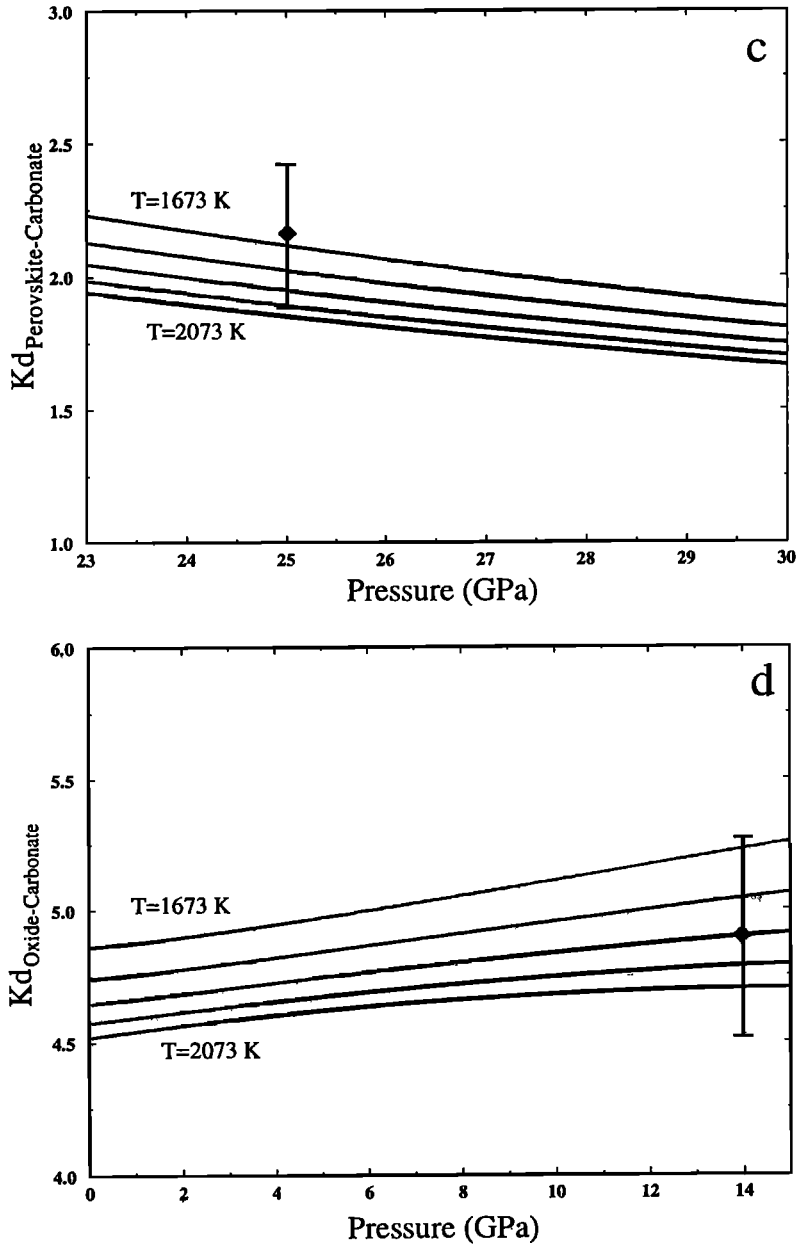

Figure 8. (continued)

Magnesite-pyroxene or magnesite-olivine experiments are thus pertinent for determining the stability limits of solid carbonates in the mantle, as well as to discuss the composition of CO_2-rich melts at great depths. The experiments performed in the pseudobinary magnesite-pyroxene and magnesite-olivine systems show that melting occurs close to 2023 K at 14-15 GPa. In iron-free systems, *Katsura and Ito* [1990] measured a eutectic temperature of 2093 K at the same pressure conditions. The presence of iron thus depresses the eutectic melting points in these silicate-carbonate systems by about 100 K, a value not very different from the iron-induced depression of solidus temperature in CO_2-free systems [e.g. *Herzberg et al.*, 1990]. In the more complex mantle systems, the solidus temperature is expected to be depressed by another 100-150 K [e.g., *Herzberg et al.*, 1990]. We thus infer solidus temperatures of about 1873 K for a peridotite-CO_2 system at 14-15 GPa; the presence of CO_2 thus lowers the solidus temperature of the mantle by about 400 K, a value very consistent with that obtained by comparing the results of *Herzberg et al.* [1990] and *Canil and Scarfe* [1990] in peridotite melting experiments without and with CO_2, respectively. Finally, if some water is present, *Canil and Scarfe* [1990] measured an additional depression of the melting point by about 200 K. Since temperature is believed to be close to 1673 K at such depths (400 km), there is a good possibility that progressive heating and homogenization of subducted materials in the transition zone will produce CO_2-rich melts similar to that produced in this study.

When such melting occurs, a magnesite-rich liquid is produced. This confirms that CO_2 is an incompatible element, even at depth of 400 km. An important point is that CO_2 is dissolved in the liquid in the form of carbonate $(Mg,Fe)CO_3$.

This has been shown in the experimental work of *Katsura and Ito* [1990], who first proposed a eutectic behavior in the system $MgSiO_3$-$MgCO_3$ at high pressures and temperatures. The present study confirms their result and extends it to other compositions. Melts formed in the CO_2-bearing mantle are possible candidates for explaining silica-undersaturated magmas such as kimberlites or komatiites. Several explanations have been proposed to interpret these MgO-rich magmas which include for komatiites, partial melting of mantle peridotite at 5-8 GPa [*Takahashi*, 1986], and partial melting of carbonated peridotites for kimberlites at similar pressures [*Canil and Scarfe*, 1990]. In order to compare the liquids formed in our experiments to these Mg-rich magmas, we use the ratio $r = (FeO+MgO)/SiO_2$, which should indeed be compared to the ratio of all divalent ions to SiO_2 in more complex mantle systems. In sample BT5, which might be taken as an approximation of a carbonated peridotite, $r = 1.8$. The liquid formed in this experiment thus has a higher r than usually found in kimberlites, for which r is about 1.3 [e.g., *Dawson*, 1980]. This is in good agreement with the study of *Canil and Scarfe* [1990], who showed that for pressures above 9 GPa, melting in the peridotite + CO_2 system produces liquids which are too Mg-rich relative to kimberlite. In contrast, for experiments performed in the pyroxene-magnesite system, an average value of $r = 1.2$ is found, which is similar to that in natural kimberlites. It is usually assumed that magmas formed at transition zone conditions would differentiate by crystallization of olivine during their ascent in the mantle, thus decreasing their values of r, and eventually erupt at 5-7 GPa in the form of kimberlites. Alternatively, the results of the present study in the pyroxene-carbonate system suggest that kimberlites might form at very high pressures (i.e., > 9 GPa) by melting of carbonated pyroxenites.

Acknowledgments. We wish to thank Max Schmidt for his help in preparing the cell assemblies. L. Thieblaut, D. Rubie and V. von Seckendorff are warmly acknowledged for providing the synthetic enstatite $MgSiO_3$, the San Carlos olivine and the synthetic $(Fe_{0.2}Mg_{0.8})SiO_3$ enstatite, respectively. Jianzhong Zhang and Bruno Reynard are warmly acknowledged for their careful reviews, and B.J. Wood for helpful suggestions and comments. Multianvil experiments were performed at Bayerisches Geoinstitut under the EC "Human Capital and Mobility-Acess to Large Scale Facilities" programme (contract ERBCHGECT940053 to D.C. Rubie).

References

Becker, H., and R. Altherr, Evidence from ultra-high-pressure marbles for recycling of sediments into the mantle, *Nature*, *358*, 745-748, 1992.

Biellmann, C., P. Gillet, F. Guyot, J. Peyronneau and B. Reynard, Experimental evidence for carbonate stability in the Earth's lower mantle, *Earth Planet. Sci. Lett.*, *118*, 31-41, 1993.

Brey, G., W.R. Brice, D.J. Ellis, D.H. Green, K.L. Harris, and I.D. Ryabchikov, Pyroxene-carbonate reactions in the upper mantle, *Earth Planet Sci. Lett.*, *62*, 64-74, 1983.

Canil, D., and C.M. Scarfe, Phase relations in peridotite + CO_2 systems to 12 GPa: Implications for the origin of kimberlite and carbonate stability in the Earth's upper mantle, *J. Geophys. Res.*, *95*, 15,805-15,816, 1990.

Dalton, J.A., and B.J. Wood, The partitioning of Fe and Mg between olivine and carbonate and the stability of carbonate under mantle conditions, *Contrib. Mineral. Petrol.*, *114*, 501-509, 1993.

Dawson, J.B., Kimberlites and their xenoliths, in *Mineral and Rocks*, 252 pp., Spingler-Verlag, New York, 1980.

Fei, Y., H.-K. Mao, and B. Mysen, Experimental determination of element partitioning and calculation of phase relations in the MgO-FeO-SiO_2 system at high pressure and high temperature, *J. Geophys. Res.*, *96*, 2157-2169, 1991.

Fiquet G., D. Andrault, A. Dewaele, T. Charpin, M. Kunz and D. Haüsermann, P-V-T equation of state of $MgSiO_3$-perovskite, *Phys. Earth Planet. Int.*, in press, 1997.

Guyot F., Y. Wang, Ph. Gillet and Y. Ricard, Quasi-harmonic computations of thermodynamic parameters of olivines at high-pressure and high-temperature. A comparison with experiment data, *Phys.Earth Planet. Int.*, *98*, 17-29, 1996.

Herzberg, C., T. Gasparik and H. Sawamoto, Origin of mantle peridotite: Constraints from melting experiments to 16.5 GPa, *J. Geophys. Res.*, *95*, 15,779-15,803, 1990.

Herzberg, C., and J. Zhang, Melting experiments on anhydrous peridotite KLB-1: Compositions of magmas in the upper mantle and transition zone, *J. Geophys. Res.*, *101*, 8271-8295, 1996.

Irving, A.J., and P.J. Wyllie, Subsolidus and melting relationships for calcite, magnesite and the join $CaCO_3$-$MgCO_3$ to 36 kb, *Geochim. Cosmochim. Acta*, *39*, 35-53, 1975.

Katsura, T. and E. Ito, The system Mg_2SiO_4-Fe_2SiO_4 at high pressures and temperatures: Precise determination of stabilities of olivine, modified spinel and spinel, *J. Geophys. Res.*, *94*, 15,663-15,670, 1989.

Katsura, T. and E. Ito, Melting and subsolidus relations in the $MgSiO_3$-$MgCO_3$ system at high pressures: Implications to evolution of the Earth's atmosphere, *Earth Planet. Sci. Lett.*, *99*, 110-117, 1990.

Koch-Müller, M., L. Cemic and K. Langer, Experimental and thermodynamic study of Fe-Mg exchange between olivine and orthopyroxene in the system MgO-FeO-SiO_2, *Eur. J. Mineral.*, *4*, 115-135, 1992.

Kushiro, I., H. Satake, and S. Akimoto, Carbonate-silicate reactions at high pressures and possible presence of dolomite and magnesite in the upper mantle, *Earth Planet. Sci. Lett.*, *28*, 116-120, 1975.

Lesher, C.E., and D. Walker, Cumulate maturation and melt migration in a temperature gradient, *J. Geophys. Res.*, *93*, 10,295-10,311, 1988.

Martinez, I., A. Deutsch , U. Schärer, P. Ildefonse, F. Guyot, and P. Agrinier, Shock recovery experiments on dolomite and thermodynamical calculations of impact induced decarbonation, *J. Geophys. Res.*, 100, 15,465-15,476, 1995.

Martinez, I., Y. Wang, F. Guyot, R.C. Liebermann, and J.C. Doukhan, Microstructures and iron partitioning in (Mg,Fe)SiO_3 perovskite-(Mg,Fe)O magnesiowustite assemblages: An analytical transmission electron microscopy study, *J. Geophys. Res.*, *102*, 5265-5280, 1997.

Matas, J., Y. Ricard, P. Gillet, and F. Guyot, Phase transition in the upper mantle and their geodynamical consequences, Ann. Geophys., 14, suppl. I, C39, 1996.

McFarlane, E.A., M.J. Drake, and D.C. Rubie, Element partitioning between Mg-perovskite, magnesiowüstite, and silicate melt at conditions of the Earth's mantle, *Geochim. Cosmochim. Acta*, *58*, 5161-5172, 1994.

Newton, R.C., and W.E. Sharp, Stability of forsterite + CO_2 and its bearing on the role of CO_2 in the mantle, *Earth Planet. Sci. Lett.*, *26*, 239-244, 1975.

Presnall, D.C., and T. Gasparik, Melting of enstatite ($MgSiO_3$) from 10 to 16.5 GPa and the forsterite (Mg_2SiO_4)-majorite ($MgSiO_3$) eutectic at 16.5 GPa: Implications for the origin of the mantle, *J. Geophys. Res.*, *95*, 15,771-15,777, 1990.

Saxena, S.K., N. Chatterjee, Y. Fei, and G. Shen, *Thermodynamic Data on Oxides and Silicates*, 428 pp., Springer-Verlag, New York, 1993.

Schiano P., R. Clocchiatti , N. Shimizu, D. Weis and N. Mattielli, Cogenetic silica-rich and carbonate-rich melts trapped in mantle minerals in Kerguelen ultramafic xenoliths: Implications for metasomatism in the oceanic upper mantle, *Earth Planet. Sci. Lett.*, *123*, 167-178, 1994.

Schmidt, M.W., Lawsonite: Upper pressure stability and formation of higher density hydrous phases, *Am. Mineral.*, *80*, 1286-1292, 1995.

Schrauder, M., and O. Navon, Solid carbon dioxide in a natural diamond, *Nature*, *365*, 42-44, 1993.

Sueno, S., M. Cameron, and C.T. Prewitt, Orthoferrosilite: High temperature crystal chemistry, *Amer. Mineral.*, *58*, 649-664, 1976.

Suzuki, T., and M. Akaogi, Element partitioning between olivine and silicate melt under high pressure, *Phys. Chem. Miner.*, *22*, 411-418, 1995.

Takahashi, E., Melting of a dry peridotite KLB-1 up to 14 GPa: Implications on the origin of peridotitic upper mantle, *J. Geophys. Res.*, *91*, 9367-9382, 1986.

von Seckendorff V., and H. O'Neill, An experimental study of Fe-Mg partitioning between olivine and orthopyroxene at 1173, 1273 and 1423 K and 1.6 GPa, *Contrib. Mineral. Petrol.*, *113*, 196-207, 1993.

Walter, M J., Y. Thibault, K. Wei, and R.W. Luth, Characterizing experimental pressure and temperature conditions in multi-anvil apparatus, *Can. J. Phys.*, *73*, 273-286, 1995.

Wang, Y., F. Guyot and R.C. Liebermann, Electron microscopy of (Mg, Fe)SiO_3 perovskite: evidence for structural phase transitions and implications for the lower mantle, *J. Geophys. Res.*, *97*, 12,327-12,347, 1992.

Wiser, N.M., and B.J. Wood, Experimental determination of activities in Fe-Mg olivine at 1400 K, *Contrib. Mineral. Petrol.*, *108*, 146-153, 1991.

E.-M. Chamorro Peréz, P. Gillet, J. Matas, and G. Vidal, Laboratoire des Sciences de la Terre, Ecole Normale Supérieure de Lyon, 46, allée d'Italie, 69364 Lyon cedex 07, France.

I. Martinez, Laboratoire de Géochimie des isotopes stables, Institut de Physique du Globe, 4, place Jussieu, 75251 Paris cedex 05, France. (e-mail: martinez@ipgp.jussieu.fr)

(Received June 23, 1997; revised October 31, 1997; accepted November 18, 1997.)